ARTICLES
https://doi.org/10.1038/s41928-018-0101-5
nature electronics

Single-crystalline layered metal-halide perovskite nanowires for ultrasensitive photodetectors

Jiangang Feng[1,2,8], Cheng Gong[3,8], Hanfei Gao[1,2], Wen Wen[2,4], Yanjun Gong[2,5], Xiangyu Jiang[1], Bo Zhang[6], Yuchen Wu[1]*, Yishi Wu[5], Hongbing Fu[7]*, Lei Jiang[1,2,6] and Xiang Zhang[3]*

Metal-halide perovskites have long carrier diffusion lengths, low trap densities and high carrier mobilities, and are therefore of value in the development of photovoltaics and light-emitting diodes. However, the presence of thermally activated carriers in the materials leads to high noise levels, which limits their photodetection capabilities. Here, we show that ultrasensitive photodetectors can be created from single-crystalline nanowire arrays of layered metal-halide perovskites. A series of nanowires was fabricated in which layer-by-layer self-organization of insulating organic cations and conductive inorganic frameworks, along the nanowire length, creates high resistance in the interior of the crystals and high conductivity at the edges of the crystals. Using these structures, high-performance photodetection was achieved with responsivities exceeding 1.5×10^4 A W^{-1} and detectivities exceeding 7×10^{15} jones. Our state-of-the-art device performance originates from a combination of efficient free-carrier edge conduction and resistive hopping barriers in the layered perovskites.

Metal-halide perovskites are promising materials for optoelectronic devices such as solar cells and light-emitting diodes[1–8]. These materials offer low-cost solution processibility, highly efficient light absorption, tunable electronic bandgap and long carrier diffusion length[1–4]. However, the air- and photoinstability of three-dimensional (3D) metal-halide perovskites has limited the long-term commercial viability of these materials. Two-dimensional (2D) layered perovskites have emerged as a more stable alternative. These perovskites are based on quantum wells consisting of alternating layers of inorganic perovskites (wells) and bulk organic spacers (barriers), and the halide perovskites are protected by organic cationic layers, resulting in enhanced stability[9–21].

Progress in the development of photodetection based on perovskites has been limited primarily by trade-offs in responsivity, detectivity and response rate[22–25]. The fundamental issue is that a high photocurrent requires materials with excellent crystallinity for efficient charge conduction[26–28], and a low dark current demands a large population of either defects or barriers to inhibit the transport of thermally excited carriers[29]. Thus, there appears to be an inherent paradox to combine both high resistance for suppressed dark currents and good conduction for enhanced photocurrents in single-phase materials. For example, high photocurrents and high dark currents are harvested simultaneously in 3D single-crystalline perovskites[26–28], whereas low photocurrents and low dark currents coexist in polycrystalline perovskite films due to the presence of grain boundaries that act as scattering centres[30,31].

Two-dimensional Ruddlesden–Popper layered perovskites are promising materials for photodetection due to their highly anisotropic structure that integrates both intra-well charge conductive channels and resistive hopping barriers in orthogonal orientations[9–21]. However, challenges remain in the selective inhibition of dark current and enhancement of photocurrent along the direction of charge transport. Exotic edge states in 2D Ruddlesden-Popper perovskites were recently discovered, which enable rapid dissociation of bound excitons and sustain long-lived free carriers[13]. This edge characteristic creates new possibilities to crosslink the intra-well exciton formation to orthogonal free-carrier edge conduction.

In this Article, we designed and fabricated 2D-perovskite nanowire arrays (Ruddlesden–Popper layered perovskites of $(BA)_2(MA)_{n-1}Pb_nI_{3n+1}$, where BA = butylammonium, MA = methylammonium, and n = layer number, 2–5 in this study) with a pure (101) crystallographic orientation. Each wire length is oriented perpendicular to the perovskite layers, and the spatially confined height and width are parallel to the perovskite layer. The geometry was designed based on three considerations: a tens of micrometres channel length consists of thousands of serial hopping barriers that largely suppress the dark current; excitons efficiently diffuse to the edge along short-length single-crystalline perovskite layers and dissociate into long-living free carriers for boosted photocurrent; and arrays amplify the photoresponse. Compared to polycrystalline thin films (Fig. 1a)—with sub-hundred-nanometre crystallites, large-quantity surface defects and grain boundaries—single-crystalline nanowires allow efficient charge transport in well layers (Fig. 1b). With photon (hv) input, the high number of exposed layer edges can efficiently dissociate tightly bound excitons into free carriers, which provides a channel for generating and conducting photocarriers (Fig. 1c). Additionally, the layer edges concentrate photocarriers from the crystal interior to the surface, which results in direct carrier injection to the top-contact electrodes. Thus, our device design enables a high resistance for suppressing the dark current and a high-photoconductivity channel. Based on the nanowire arrays, we demonstrated photodetectors with state-of-the-art figures of merit,

[1]Key Laboratory of Bio-inspired Materials and Interfacial Science, Technical Institute of Physics and Chemistry, Chinese Academy of Sciences, Beijing, China. [2]University of Chinese Academy of Science, Beijing, China. [3]Nano-scale Science and Engineering Center (NSEC), University of California, Berkeley, CA, USA. [4]CAS Center for Excellence in Nanoscience, CAS Key Laboratory of Standardization and Measurement for Nanotechnology, National Center for Nanoscience and Technology, Beijing, China. [5]Beijing National Laboratory for Molecules Science (BNLMS), State Key Laboratory for Structural Chemistry of Unstable and Stable Species & Key Laboratory of Photochemistry, Institute of Chemistry, Chinese Academy of Sciences, Beijing, China. [6]School of Chemistry, Beihang University, Beijing, China. [7]Tianjin Key Laboratory of Molecular Optoelectronic Sciences, Collaborative Innovation Center of Chemical Science and Engineering (Tianjin), Department of Chemistry, Tianjin University, Tianjin, China. [8]These authors contributed equally: Jiangang Feng, Cheng Gong. *e-mail: wuyuchen@iccas.ac.cn; hongbing.fu@tju.edu.cn; xiang@berkeley.edu

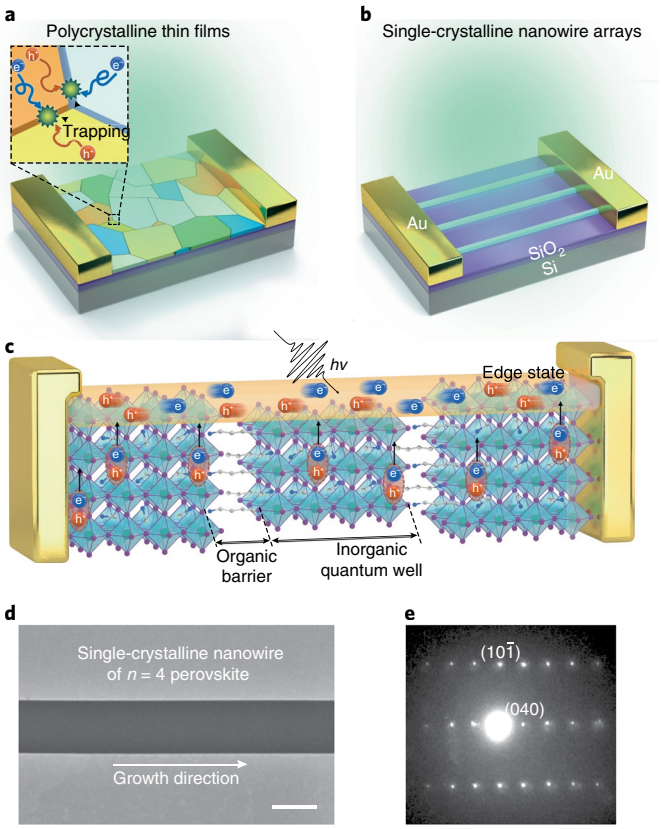

Fig. 1 | Schematics of 2D-perovskite photodetectors. a,**b**, Illustration of photodetectors based on polycrystalline thin films (**a**) and single-crystalline nanowire arrays (**b**) of 2D perovskites. Abundant grain boundaries and surface defects in polycrystalline thin films can suppress the photocurrent of devices by trapping, scattering and recombination of photoexcited carriers (inset in **a**). **c**, Scheme of carrier dynamics in the photodetector of single-crystalline (101)-oriented 2D perovskite. This device design integrates insulating organic barriers in the carrier-transport pathway for suppressing the dark current with a highly photoconductive channel, provided by the exposed crystalline edges, for exciton dissociation, free-carrier conduction and charge injection. **d**, Representative TEM image of a single-crystalline nanowire of $n=4$ 2D perovskite. Scale bar, 500 nm. **e**, Corresponding SAED pattern of the nanowire.

including average responsivities of more than 1.5×10^4 A W^{-1} and detectivities of more than 7×10^{15} jones.

Development of layered-perovskite nanowires

We fabricated 2D-perovskite nanowire arrays through a capillary-bridge rise approach on an asymmetric-wettability topographical template (see Supplementary Figs 1, 2 and Supplementary Note 1 for details). The crystal structure of synthesized 2D perovskites is confirmed by X-ray diffraction (XRD) and indexed as pure phase with layer numbers of 2–5 (Supplementary Fig. 3)[32]. Capillary-bridge rise experiments were carried out by combining an asymmetric-wettability template with the target substrate (see experimental details in Supplementary Fig. 4 and Supplementary Note 2) and the underlying mechanism was explained by lattice Boltzmann method simulations (Supplementary Figs. 5, 6).

The transmission electron microscopy (TEM) image of a nanowire of $n=4$ 2D perovskite in Fig. 1d shows no detectable grain boundary, indicating its single-crystalline nature. The corresponding selected area electron diffraction (SAED) pattern (Fig. 1e) presents sharp diffraction spots, assigned to the [040] and [10$\bar{1}$] zone axes, revealing the high crystallinity of the nanowire with a preferential growth direction along the (010) orientation. Strict alignment, precise position and homogeneous size of nanowire arrays (Fig. 2a, Supplementary Fig. 7) are revealed by morphological characterization under scanning electron microscopy (SEM). The low-magnification SEM images (Supplementary Fig. 8) depict high-quality nanowire arrays over a large area. To characterize the crystallographic orientation over the macroscopic scale, XRD and grazing incidence wide-angle X-ray scattering (GIWAXS) analyses were performed on nanowire arrays. The presence of only (111), (202) and (313) peaks in the XRD diagram (Supplementary Fig. 9a) and discrete diffraction spots in the GIWAXS patterns (Fig. 2b, Supplementary Fig. 9c,d), which can be assigned to (101)-oriented 2D perovskites, indicates the pure crystallographic orientation of nanowires. For $n=2$ perovskites, mixed (101) and (010) crystallographic orientations were observed (Supplementary Fig. 9a,b). The X-ray and electron diffraction results demonstrate that the single-crystalline nanowires of $n=3$–5 perovskites are self-organized with alternating layers of semiconducting wells and insulating barriers along the growth direction of the nanowires, while exposing abundant edges on the surface. In contrast, the thin films fabricated by the spin-coating method feature lower crystallinity, small crystallite sizes and ubiquitous grain boundaries (Supplementary Fig. 10).

The absorption spectra of $n=3$–5 perovskite nanowires manifest redshift absorption edges ranging from 1.6–1.8 eV, in striking contrast to a sole absorption peak at 2.18 eV in $n=2$ perovskites (Fig. 2c). The photoluminescence (PL) spectra (Fig. 2d) also illustrate a marked difference between $n=2$ and $n=3$–5 perovskites: the PL peak at 2.05 eV of $n=2$ nanowires corresponds to the band-edge radiative recombination, whereas the PL emissions range from 1.6 to 1.7 eV for $n=3$–5 perovskites. By performing confocal PL mapping on exfoliated crystals (see experimental details in Supplementary Note 3), we validate the low-energy PL emissions localized at the layer edges (that is, from edge states) in $n=3$–5 perovskites, whereas the crystal interiors exhibit higher-energy emissions (Supplementary Fig. 11). The coincidence of photon emissions from nanowires and edge states suggests that the layer edges dominate the photon emissions in nanowires of $n=3$–5 perovskites. The time-resolved PL mapping illustrates that the photocarrier lifetimes localized at layer edges are longer than those in crystal interiors, indicating that the carriers localized at layer edges and in crystal interiors stem from two different energy levels (Supplementary Fig. 12).

To identify the essence of photogenerated species, we monitored the excitation-power-dependent PL emissions of exfoliated crystal interiors and nanowires (Supplementary Fig. 13). The integrated PL intensities of crystal interiors and nanowires follow the power law, $I(P)\sim P^{\alpha}$, where $I(P)$ is the integrated PL intensity at the excitation power P, and α is a coefficient. The crystal interiors of $n=2$–5 perovskites exhibit high-energy PL emissions with near-unity α values (Fig. 2e), revealing the monomolecular exciton recombination in crystal interiors. These results are rationalized by the relatively large exciton binding energy, exceeding 200 meV in 2D perovskites[9,13]. In stark contrast, the $n=3$–5 perovskite nanowires manifest lower-energy emission (1.6–1.7 eV) with α values ranging from 1.4 to 1.8, which evidences the emergence of bimolecular free-carrier recombination (Fig. 2f)[13,33,34].

Given that the layer edges are located on the surfaces of nanowires and that photogenerated excitons in crystal interiors possess a limited diffusion length (determined as 152.2 ± 8.2 nm, Supplementary Note 4, Supplementary Figs. 14, 15, Supplementary Table 1), we measured PL emissions and photocurrents of nanowires with different cross-sectional sizes. A series of wires with heights in the range 0.15–1.5 μm and widths in the range 0.4–10.5 μm was fabricated by tuning the widths of micropillars and the concentrations of precursor solutions (Supplementary Figs. 16, 17). Height-dependent PL emissions are observed in $n=4$ wires (Fig. 2g, Supplementary Fig. 18):

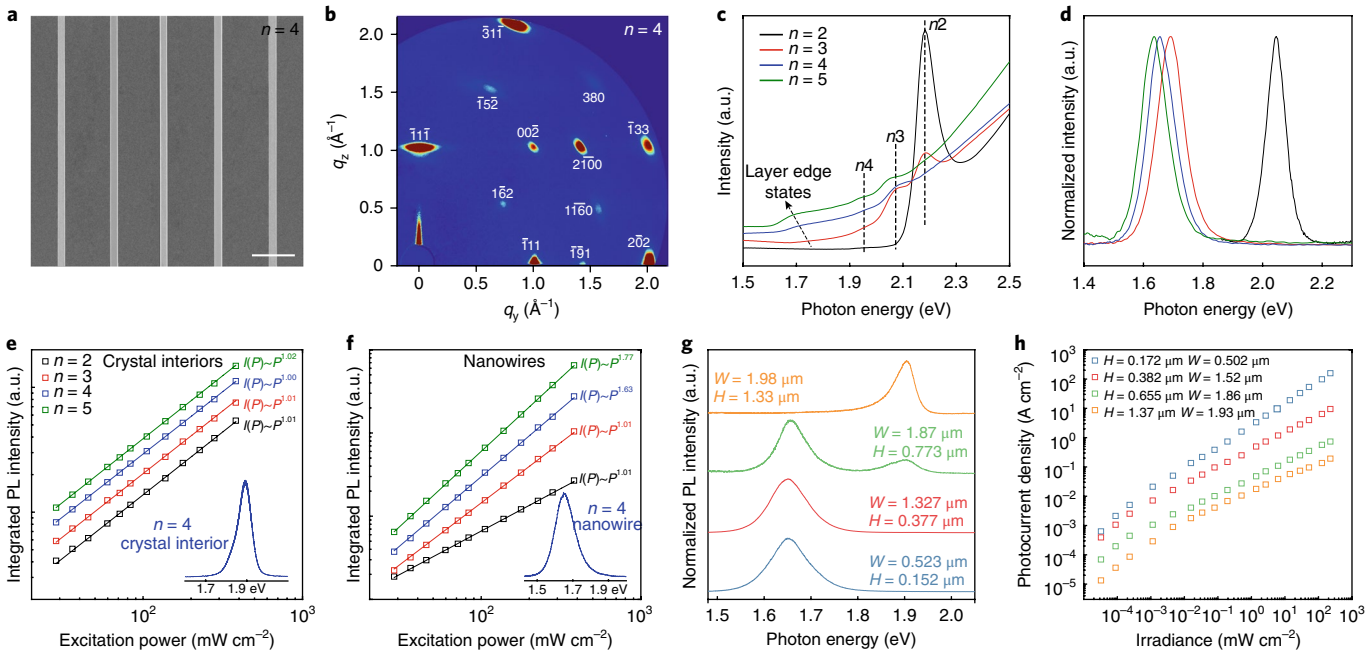

Fig. 2 | Single-crystalline 2D-perovskite nanowires with free-carrier generation at layer edges. a, SEM image of $n=4$ perovskite nanowire arrays, which presents strict alignment, precise position and homogenous size of nanowires. **b**, GIWAXS pattern of $n=4$ nanowires. The discrete diffraction spots can be assigned to $n=4$ perovskite with the (101) crystallographic orientation. **c**,**d**, Absorption and photoluminescence (PL) spectra, respectively, of $n=2$–5 nanowire arrays. In striking contrast to $n=2$ perovskites, the $n=3$–5 perovskite nanowires manifest redshift absorption edges at 1.6–1.8 eV and redshift PL peaks centred at 1.6–1.7 eV, which signal the presence of edge states. **e**,**f**, Excitation-power-dependent integrated PL intensities recorded on exfoliated crystal interiors (**e**) and nanowires (**f**) of $n=2$–5 perovskites. Insets present representative PL spectra of crystal interiors and nanowires of $n=4$ perovskites. The integrated intensities of PL emission follow a power law, $I(P) \sim P^{\alpha}$, where $I(P)$ represents the integrated PL intensity at the excitation power, P, and α is a coefficient. The near-unity α values indicate only the presence of monomolecular excitonic recombination in exfoliated crystal interiors, while α values ranging from 1.4 to 1.8 in nanowires of $n=3$–5 perovskites evidence the emergence of bimolecular free-carrier recombination. **g**, PL emission of $n=4$ perovskite nanowires with different sizes. The weight of excitonic emission at 1.9 eV increases with increasing wire height, indicating that the layer edges located on the surface of wires dominate the dissociation of excitons and generation of free carriers. **h**, Photocurrent density of $n=4$ perovskite nanowires with different sizes. With increasing wire height, the dramatic fall of photoconductivity, together with the rise in the exciton population, suggests that free carriers localized at layer edges, instead of excitons in crystal interiors, dominate the photoconduction.

for a wire of less than 200 nm in height, a single PL peak centred at 1.65 eV can be detected; with the increase of wire height, the high-energy excitonic emissions at 1.90 eV become more recognizable; as the height exceeds 1 μm, the excitonic emissions dominate the PL spectra.

The height dependence of PL emission provides unambiguous evidence of exciton dissociation into free carriers at the layer edges of nanowires. First, the possible mechanism of carrier transfer from low- to high-layer perovskites can be clearly ruled out for the low-energy PL emissions in wires, owing to the lack of height dependence[17,19]. Second, the height response indicates competition between the exciton recombination in crystal interiors and exciton dissociation at the layer edges located on the surfaces of wires. For wires with heights comparable to the exciton diffusion length, excitons generated in crystal interiors can be effectively concentrated at layer edges and then dissociate into free carriers, and thus edge-state emissions. In contrast, for wires with heights far exceeding the exciton diffusion length, the excitons recombine and emit high-energy photons in crystal interiors before diffusing onto surfaces. To validate this mechanism, we further compared the PL emissions in both the presence and absence of electron quenchers on wires with different heights (Supplementary Fig. 19). The PL intensities at 1.65 eV experience a sharp drop after the addition of a quencher layer, whereas the populations of high-energy excitons are less susceptible to the quenchers, suggesting that low-energy photocarriers are concentrated on the surfaces and high-energy photocarriers are located in crystal interiors.

To evaluate the role of edge states on carrier transport, we characterized the height-dependent photocurrents of perovskite wires. By increasing the height from 0.17 to 1.37 μm, the photocurrent densities of $n=4$ perovskite wires undergo a two orders of magnitude decrease (Fig. 2h, Supplementary Fig. 20). The observation of low photocurrents, together with exciton-dominated PL emission in thick wires, suggests that excitons in crystal interiors contribute little to the photoconductivity. In other words, the edge states dominate the dissociation of excitons, and production and transport of free carriers for 2D-perovskite nanowires. We also compared the photocurrent densities of $n=2$ perovskite wires with different sizes (Supplementary Fig. 21). The inconspicuous height dependence of photoconductivity for $n=2$ perovskites with only excitons confirms the importance of edge states in free carrier transport.

Ultrasensitive photodetection

Based on these carefully designed and prepared nanowires, we examined the figures of merit of the photodetectors. Figure 3a presents the dark currents of nanowire photodetectors. The $n=2$–4 perovskite nanowires exhibit low dark currents below 10^{-12} A, whereas the $n=5$ nanowires present an increased dark current exceeding 10^{-10} A (Fig. 3a), comparable to its 3D counterpart[22,26]. We attribute the suppressed dark currents of 2D perovskite nanowires to the serial insulating organic barriers in

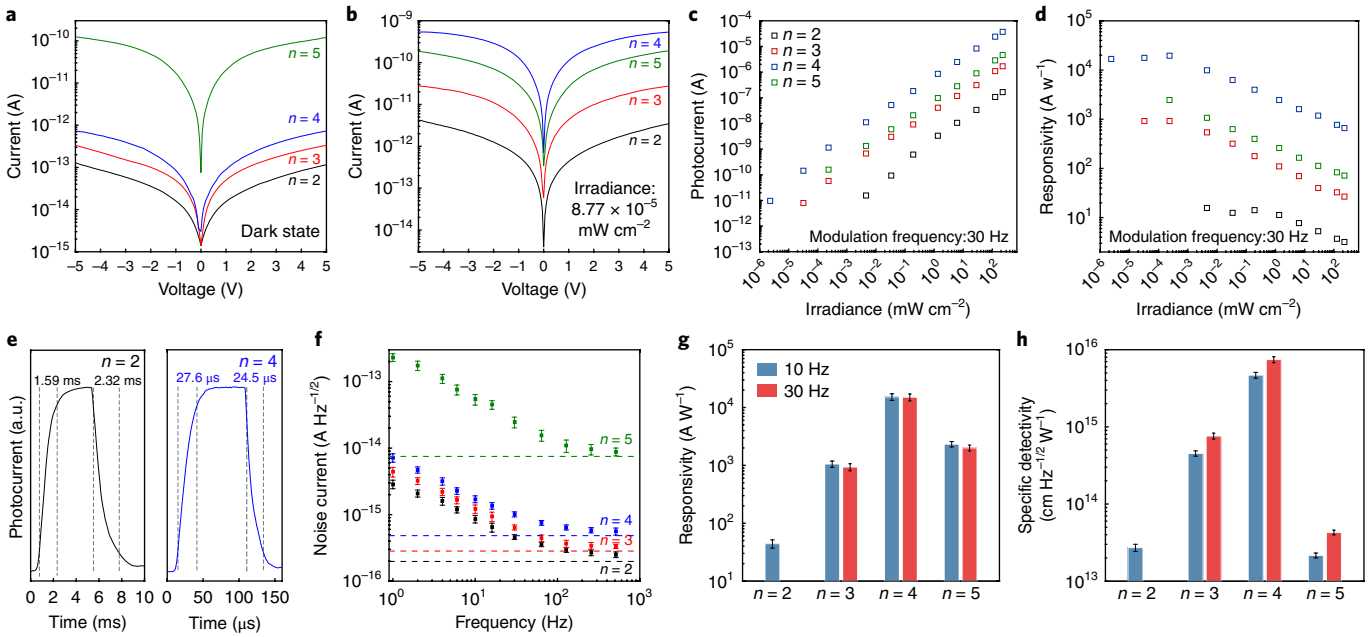

Fig. 3 | Photodetector performance of single-crystalline nanowire arrays. a,**b**, *I*–*V* curves of 2D-perovskite nanowire arrays in the dark state (**a**) and in light illumination (**b**) with an irradiant power of 8.77×10^{-5} mW cm^{-2}. The low dark currents of $n=2$–4 perovskite nanowires suggest large serial resistances are induced by the organic barriers. **c**,**d**, Irradiance-dependent photocurrent (**c**) and responsivity (**d**) of 2D-perovskite nanowire arrays measured under a modulation frequency of 30 Hz. Improved responsivity at $n=3$–5 perovskite can be attributed to the efficient exciton dissociation, free-carrier conduction and charge injection at crystalline edges. **e**, Temporal response of 1D arrays of layered perovskites with $n=2$ and 4. **f**, Frequency-dependent noise current at a voltage bias of 5 V. The noise current is dominated by 1/*f* noise at low frequency, which achieved the shot noise limit at around 100 Hz. The points correspond to average values of ten measurements on the same device for each 2D-perovskite nanowire, and the error bars represent the standard deviation. **g**,**h**, Statistics of responsivities and detectivities, respectively, of $n=2$–5 nanowires under modulation frequencies of 10 Hz and 30 Hz. The average detectivity is $(7.45\pm0.66)\times10^{15}$ jones for $n=4$ perovskite nanowires at 30 Hz. Statistics for $n=2$–5 perovskite photodetectors are calculated on the basis of 10 devices (Supplementary Fig. 27).

the carrier-transport channels, which is evidenced by the pure (101) crystallographic orientation with alternating wells and barriers along the growth direction. The steep increase of dark current in $n=5$ nanowires might be caused by the reduced number of barriers in the channel and increased defect populations, reflected by the poorer diffraction signals (Supplementary Fig. 9d) and higher measured trap density (Supplementary Figs. 22, 23). Under light illumination, the $n=4$ perovskites manifest the highest photocurrents (Fig. 3b). The dramatic increase of photocurrents for $n=3$–5 nanowires compared to the $n=2$ nanowires highlights the essential role of layer edges for free-carrier generation and transport in achieving high photoconductivity.

To measure the responsivities and specific detectivities of photodetectors, we monitored the photocurrents under frequency-modulated light illumination (see Methods). Representative frequency responses of currents under different irradiances are displayed in Supplementary Fig. 25. The lowest measured irradiance achieves 2.33×10^{-6} mW cm^{-2} for $n=4$ nanowire photodetectors, corresponding to a light power of 0.58 fW with an operating area of around 25 µm^2. The slow response restricts $n=2$ nanowires for frequency-modulated photodetection under low irradiances, whereas the detectable irradiance of $n=5$ devices is limited to 2.37×10^{-4} mW cm^{-2} owing to the large dark current. The photocurrents at a modulation frequency of 30 Hz for $n=2$–5 perovskite nanowires are presented in Fig. 3c and the responsivities (Fig. 3d) are calculated by $R=I_{ph}/P$, where I_{ph} is the photocurrent and P is the illumination power. Under an irradiance of less than 10^{-3} mW cm^{-2}, the photocurrents exhibit a linear response to irradiances, giving rise to irradiance-independent saturated responsivities (Fig. 3c,d, Supplementary Fig. 24). Under irradiances exceeding 10^{-3} mW cm^{-2}, we observed a fall in the responsivities and the rise of 3 dB frequencies (Supplementary Fig. 25), suggesting the filling of traps and enhancement of many-body effects shorten the lifetimes of excitons and free carriers under high irradiances, and hence the loss of photoconductive gain but the promotion of response speed. The response time of the $n=4$ nanowire devices was determined as 27.6 µs for rise and 24.5 µs for decay under an irradiance of 229 mW cm^{-2} (Fig. 3e), which is much faster than that exceeding 1 ms for $n=2$ nanowires and that for $n=3$ and 5 perovskite nanowires (Supplementary Fig. 26).

With the synergy of suppressed dark currents and boosted photocurrents in 2D-perovskite nanowires, we evaluated the specific detectivity by determining the noise. The noise currents of $n=2$–5 perovskite nanowires (Fig. 3f) are dominated by 1/*f* noise in the low-frequency region and approach the shot noise limit, $I_{shot}=(2eI_{dark})^{1/2}$, where e is the elementary charge, I_{dark} the dark current, at high frequency. Compared to $n=5$ nanowires, photodetectors based on $n=2$–4 perovskite nanowires manifest strikingly lower noise currents, which is in good accordance with their low dark currents. To evaluate the average responsivities and detectivities of each device, we assessed the statistics of device performance by measuring frequency-modulated photocurrents under their lowest achievable irradiances from 10 different devices (Supplementary Fig. 27). The specific detectivity, D^*, can be extracted using $D^*=R(AB)^{1/2}/i_{noise}$, where A is the operating area of the device, B the bandwidth and i_{noise} the noise current. The detectivities are calculated by taking the responsivities and noise currents modulated at 10 and 30 Hz (Fig. 3g,h). The $n=4$ perovskite nanowires present high average responsivities of $(1.53\pm0.19)\times10^4$ and $(1.51\pm0.21)\times10^4$ A W^{-1}, corresponding to detectivities of $(4.68\pm0.41)\times10^{15}$ and $(7.45\pm0.66)\times10^{15}$ jones (cm Hz$^{1/2}$ W^{-1}) at

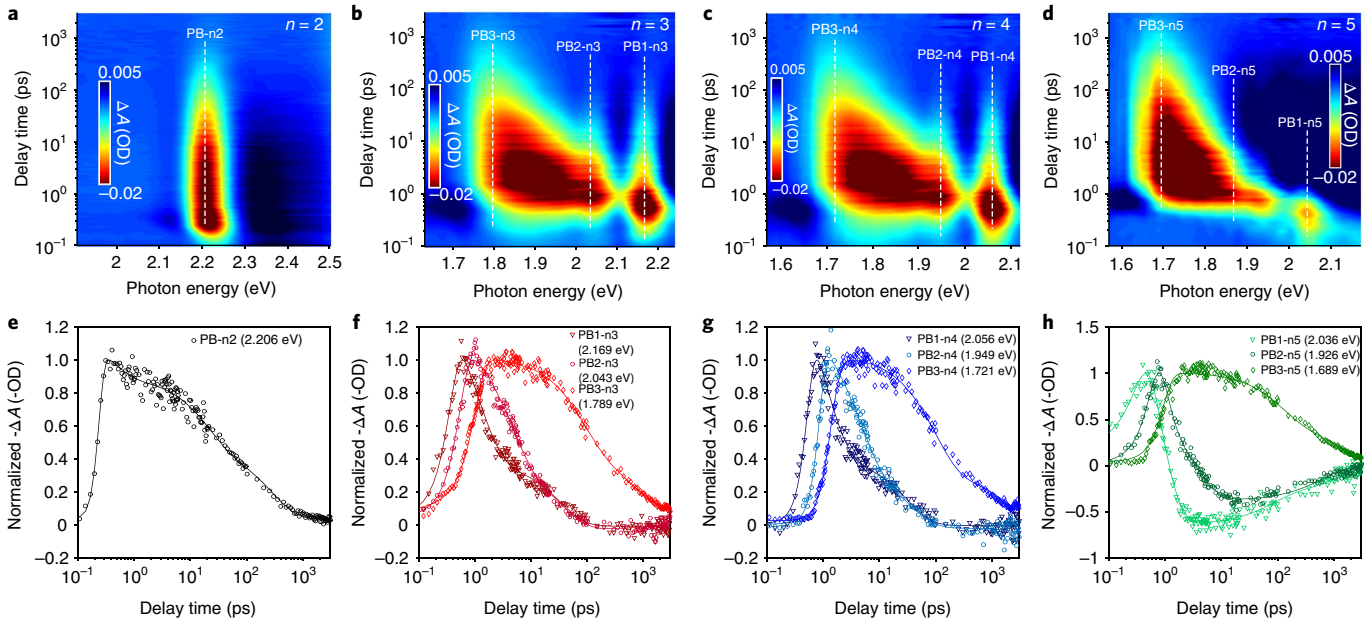

Fig. 4 | Transient absorption for 2D-perovskite single-crystalline nanowire arrays. a–d, Pseudocolour transient absorption (TA) spectra of $n=2$ (**a**), $n=3$ (**b**), $n=4$ (**c**) and $n=5$ (**d**) perovskite nanowires. For $n=2$, a photobleaching at PB-n2 (2.206 eV) dominates the TA spectra. For $n=3$ to 5, time-dependent TA spectra exhibit a cascade energy transfer from higher-energy states to lower-energy states. **e–h**, Kinetics traces of nanowire arrays of 2D perovskites. The rise of lower-energy PB3 synchronized with the ultrafast decay of higher-energy PB1 and PB2 indicates energy transfer from excitons in crystal interiors to free carriers localized at layer edges.

modulation frequencies of 10 and 30 Hz, respectively. Due to the low noise and considerable photocurrents, the reproducible detectivity of $(7.45\pm0.66)\times10^{15}$ jones represents record-high sensitivity for perovskite photodetectors (Supplementary Table 3). The detectivities of 2D-perovskite nanowires are two orders of magnitude higher than commercially available silicon photodiodes (Supplementary Table 3). Compared to the nanowire arrays, the thin films present much lower photocurrents and responsivities (Supplementary Fig. 28), which can be attributed to carrier recombination and scattering at grain boundaries, thus highlighting the significance of fabricating high-quality single-crystalline structures.

Photocarrier dynamics

To gain insights into the photophysics of single-crystalline nanowires of 2D perovskites, we monitored the energy transfer from excitons to free carriers by transient absorption (TA). In stark contrast to $n=2$ nanowires with a single photobleaching (PB) peak (Fig. 4a, Supplementary Fig. 29), TA spectra of nanowires of $n=3$–5 perovskites depict three resolvable PB peaks (Fig. 4b–d, Supplementary Fig. 29). The high-energy PB peaks on $n=3$–5 perovskite nanowires undergo a fast decay, while a broad low-energy PB peak (labelled as PB3) presents a slow decay and a continuous redshift to 1.6–1.7 eV, which signals the localization of photoexcited species from crystal interiors to layer edges. Figure 4e–h displays the kinetic traces of different PB inclusions on single-crystalline 2D-perovskite nanowires. Ultrafast decay of PB1 and PB2 inclusions presents fitted lifetimes of less than 5 ps for $n=3$–5 perovskite nanowires, in accordance with the rapid rise of PB3 within 2 ps. The decay of PB1 and PB2 inclusions is completed within 100 ps, followed by longer-lifetime carrier recombination at the low-energy layer-edge states (Fig. 4e–h, Supplementary Fig. 30, Supplementary Table 2). The essence of carriers was further identified by evaluating the evolution of reciprocal differential absorption (ΔA^{-1}) with delay time. According to the model established by Manser et al.[35], ΔA^{-1} is expected to be a linear function of delay time for the geminate free-carrier recombination. The value of ΔA^{-1} detected at low-energy photobleaching of $n=3$–5 perovskite nanowires manifests a linear dependence on delay time (Supplementary Fig. 31), which is akin to the results on 3D $CH_3NH_3PbI_3$ perovskite with a typical free-carrier nature (Supplementary Fig. 32), suggesting the effective dissociation of excitons at layer edges. The ultrafast dissociation of excitons to generate free carriers at layer edges is responsible for the high-performance photodetectors.

Conclusions

We have demonstrated high-performance photodetectors with high responsivity, detectivity and speed by developing single-crystalline 2D-perovskite nanowire arrays with a pure crystallographic orientation. High average responsivities of 1.5×10^4 A W^{-1}, detectivities of more than 7×10^{15} jones and response timed of around 25 μs have been integrated on a single device based on $n=4$ perovskite nanowires. Through the characterizations of crystal structure, photophysics and device performance, we demonstrate that 2D-perovskite nanowires are promising photodetection materials, which combine insulating organic barriers for suppressing the dark currents and high-photoconductivity crystal edges for efficient exciton dissociation, free-carrier generation and transport.

Methods

Fabrication of 1D layered-perovskite single-crystal arrays. The layered-perovskite crystals with different compositions were synthesized according to ref. [32]. Topographical templates were prepared by reactive ion-etching and the asymmetric wettability was achieved through a selective modification process (Supplementary Note 1, Supplementary Figs. 1, 2). The capillary-bridge rise assembly system was constructed by contacting a topographical template and a flat substrate to the perovskite solution (schematic illustration in Supplementary Fig. 4). The detailed discussion and the lattice Boltzmann method simulation results are presented in Supplementary Figs. 5, 6 and Supplementary Note 2.

Characterizations. The morphology of 1D single-crystal arrays was characterized by SEM (Hitachi, S-4800, Japan). AFM topography was carried out on a Bruker MultiMode 8 Atomic Force Microscope. The TEM characterizations were performed on a FEI Tecnai G20 operating at an accelerating voltage of 100 kV. X-ray diffraction of 1D arrays and powders of layered perovskites

were measured on a Bruker D8 diffractometer with monochromatized Cu K_α radiation ($\lambda = 1.5406$ Å). The GIWAXS patterns were collected on the Beijing Synchrotron Radiation Facility with an incidence angle of 0.2°. The indexing of the GIWAXS diffraction spots was carried out on GIXSGUI[36] using lattice parameters of layered perovskites from ref. [32]. The steady-state optical absorption was characterized on a Shimadzu UV-3600 spectrometer. The power-dependent PL emission was performed on an optical microscope equipped with a ×50, 0.9 numerical aperture (NA) objective and a 514-nm continuous-wave laser as excitation source. The laser beam size was optimized to a beam waist of around 5 µm to uniformly excite the nanowires. The excitation power was tuned by a neutral density filter (Thorlabs, NDC-50C-4M) and calibrated by an optical power meter (Thorlabs, PM100D).

Photodetector characterizations. For photodetection measurements, the 2D-perovskite single-crystalline nanowire arrays were fabricated from 5 mg ml^{-1} precursor solutions and micropillars in 2-µm width on 300-nm SiO_2/Si substrates. Cr/Au (10 nm/100 nm) was evaporated onto these 1D arrays as electrodes using a shadow mask. The channel length and width were controlled at 10 µm and 40 µm, respectively. The active area of device is around $10 \times 2.5\ \mu m^2$ for 4–5 nanowires covered by a pair of electrodes. The *I–V* measurements were performed using a Keithley 4200 semiconductor characterization system and a manual probe station (Lake Shore) in a vacuum of 10^{-5} torr at room temperature. The responsivity and detectivity were measured under frequency modulation. A 530-nm light-emitting diode (LED) (Thorlabs M530L3) was modulated by a function generator (Tektronix AFG1062) to illuminate the device. The light irradiance was controlled by a LED controller (Thorlabs DC2200) and calibrated by means of a silicon photodiode (Thorlabs, S130C). The device was connected in series with a 2-kΩ load resistor and a 5-V bias was applied by a Keithley 4200. The photocurrent was recorded by measuring the voltage across the resistor by means of a lock-in amplifier (Stanford Research Systems, SR830). The temporal response measurements were performed on a digital oscilloscope (Tektronix DPO 4104) under a 5-V bias. The noise currents of photodetectors were characterized with a lock-in amplifier (SR830) under darkness.

Femtosecond transient absorption spectroscopy. A Ti:sapphire femtosecond laser system provided laser pulses for the femtosecond transient absorption measurements. A regenerative amplifier (Spectra Physics, Spitifire) seeded with a mode-locked Ti:sapphire laser (Spectra Physics, Tsunami) delivered laser pulses at 800 nm (120 fs, 1 kHz), which were then divided into two components by means of a 9:1 beam splitter. The major component was sent to an optical parametric amplifier (Spectra Physics, OPA-800CF) to generate the pump pulses (400 nm 130 fs, 1 kHz). The minor component was further attenuated and focused into a 3-mm sapphire plate to generate the probe pulses. A bandpass filter (SPF-750, CVI) was inserted into the probe beam to select the visible probe (420–750 nm). The time delay between the pump and probe beams was regulated through a computer-controlled motorized translation stage in the pump beam. A magic scheme was adopted in the pump–probe measurement when necessary. The temporal resolution between the pump and the probe pulses was determined to be ~150 fs (full-width at half-maximum). The transmitted light was detected by a CMOS linear image sensor (S8377-512Q, Hamamatsu). The excitation pulsed energy was ~50 nJ as measured at the sample site. Analysis of the kinetic traces derived from time-resolved spectra was performed individually and globally using nonlinear least-squares fitting to a general sum-of-exponentials function after deconvolution of the instrument response function (IRF). All the spectroscopic measurements were carried out at room temperature.

Received: 27 November 2017; Accepted: 15 June 2018;
Published online: 13 July 2018

References

1. Stranks, S. D. et al. Electron–hole diffusion lengths exceeding 1 micrometer in an organometal trihalide perovskite absorber. *Science* **342**, 341–344 (2013).
2. Xing, G. et al. Long-range balanced electron- and hole-transport lengths in organic–inorganic $CH_3NH_3PbI_3$. *Science* **342**, 344–347 (2013).
3. Dong, Q. et al. Electron-hole diffusion lengths > 175 µm in solution-grown $CH_3NH_3PbI_3$ single crystals. *Science* **347**, 967–970 (2015).
4. Shi, D. et al. Low trap-state density and long carrier diffusion in organolead trihalide perovskite single crystals. *Science* **347**, 519–522 (2015).
5. Stranks, S. D. & Snaith, H. J. Metal-halide perovskites for photovoltaic and light-emitting devices. *Nat. Nanotech.* **10**, 391–402 (2015).
6. Sutherland, B. R. & Sargent, E. H. Perovskite photonic sources. *Nat. Photon.* **10**, 295–302 (2016).
7. Burschka, J. et al. Sequential deposition as a route to high-performance perovskite-sensitized solar cells. *Nature* **499**, 316–319 (2013).
8. Tan, Z.-K. et al. Bright light-emitting diodes based on organometal halide perovskite. *Nat. Nanotech.* **9**, 687–692 (2014).
9. Hong, X., Ishihara, T. & Nurmikko, A. V. Dielectric confinement effect on excitons in PbI_4-based layered semiconductors. *Phys. Rev. B* **45**, 6961–6964 (1992).
10. Mitzi, D. B., Wang, S., Feild, C. A., Chess, C. A. & Guloy, A. M. Conducting layered organic-inorganic halides containing <110> -oriented perovskite sheets. *Science* **267**, 1473–1476 (1995).
11. Mitzi, D. B., Feild, C. A., Harrison, W. T. A. & Guloy, A. M. Conducting tin halides with a layered organic-based perovskite structure. *Nature* **369**, 467–469 (1994).
12. Dou, L. et al. Atomically thin two-dimensional organic-inorganic hybrid perovskites. *Science* **349**, 1518–1521 (2015).
13. Blancon, J.-C. et al. Extremely efficient internal exciton dissociation through edge states in layered 2D perovskites. *Science* **355**, 1288–1292 (2017).
14. Tsai, H. et al. High-efficiency two-dimensional Ruddlesden–Popper perovskite solar cells. *Nature* **536**, 312–316 (2016).
15. Liao, Y. et al. Highly oriented low-dimensional tin halide perovskites with enhanced stability and photovoltaic performance. *J. Am. Chem. Soc.* **139**, 6693–6699 (2017).
16. Cao, D. H., Stoumpos, C. C., Farha, O. K., Hupp, J. T. & Kanatzidis, M. G. 2D homologous perovskites as light-absorbing materials for solar cell applications. *J. Am. Chem. Soc.* **137**, 7843–7850 (2015).
17. Yuan, M. et al. Perovskite energy funnels for efficient light-emitting diodes. *Nat. Nanotech.* **11**, 872–877 (2016).
18. Quan, L. N. et al. Tailoring the energy landscape in quasi-2D halide perovskites enables efficient green-light emission. *Nano Lett.* **17**, 3701–3709 (2017).
19. Wang, N. et al. Perovskite light-emitting diodes based on solution-processed self-organized multiple quantum wells. *Nat. Photon.* **10**, 699–704 (2016).
20. Xing, G. et al. Transcending the slow bimolecular recombination in lead-halide perovskites for electroluminescence. *Nat. Commun.* **8**, 14558 (2017).
21. Zhang, S. et al. Efficient red perovskite light-emitting diodes based on solution-processed multiple quantum wells. *Adv. Mater.* **29**, 1606600 (2017).
22. Li, F. et al. Ambipolar solution-processed hybrid perovskite phototransistors. *Nat. Commun.* **6**, 8238 (2015).
23. Dou, L. et al. Solution-processed hybrid perovskite photodetectors with high detectivity. *Nat. Commun.* **5**, 5404 (2014).
24. Lin, Q., Armin, A., Burn, P. L. & Meredith, P. Filterless narrowband visible photodetectors. *Nat. Photon.* **9**, 687–694 (2015).
25. Shen, L. et al. A self-powered, sub-nanosecond-response solution-processed hybrid perovskite photodetector for time-resolved photoluminescence-lifetime detection. *Adv. Mater.* **28**, 10794–10800 (2016).
26. Saidaminov, M. I. et al. Planar-integrated single-crystalline perovskite photodetectors. *Nat. Commun.* **6**, 8724 (2015).
27. Fang, Y., Dong, Q., Shao, Y., Yuan, Y. & Huang, J. Highly narrowband perovskite single-crystal photodetectors enabled by surface-charge recombination. *Nat. Photon.* **9**, 679–686 (2015).
28. Han, Q. et al. Single crystal formamidinium lead iodide ($FAPbI_3$): insight into the structural, optical, and electrical properties. *Adv. Mater.* **28**, 2253–2258 (2016).
29. Liu, X. et al. All-printable band-edge modulated ZnO nanowire photodetectors with ultra-high detectivity. *Nat. Commun.* **5**, 4007 (2014).
30. Wu, X. et al. Trap states in lead iodide perovskites. *J. Am. Chem. Soc.* **137**, 2089–2096 (2015).
31. de Quilettes, D. W. et al. Impact of microstructure on local carrier lifetime in perovskite solar cells. *Science* **348**, 683–686 (2015).
32. Stoumpos, C. C. et al. Ruddlesden-Popper hybrid lead iodide perovskite 2D homologous semiconductors. *Chem. Mater.* **28**, 2852–2867 (2016).
33. Yamada, Y., Nakamura, T., Endo, M., Wakamiya, A. & Kanemitsu, Y. Photocarrier recombination dynamics in perovskite $CH_3NH_3PbI_3$ for solar cell applications. *J. Am. Chem. Soc.* **136**, 11610–11613 (2014).
34. Blancon, J.-C. et al. The effects of electronic impurities and electron–hole recombination dynamics on large-grain organic–inorganic perovskite photovoltaic efficiencies. *Adv. Funct. Mater.* **26**, 4283–4292 (2016).
35. Manser, J. S. & Kamat, P. V. Band filling with free charge carriers in organometal halide perovskites. *Nat. Photon.* **8**, 737–743 (2014).
36. Jiang, Z. GIXSGUI: a MATLAB toolbox for grazing-incidence X-ray scattering data visualization and reduction, and indexing of buried three-dimensional periodic nanostructured films. *J. Appl. Cryst.* **48**, 917–926 (2015).

Acknowledgements

The authors acknowledge the National Natural Science Foundation (21703268, 21633014), the Beijing Natural Science Foundation (2182081), and the Ministry of Science and Technology (MOST) of China (2017YFA0204504).

Author contributions

J.F., C.G., Yuchen W., L.J. and X.Z. initiated the research and designed the experiments; J.F. and H.G. prepared layered-perovskite nanowire arrays; J.F. performed material characterizations, device fabrication and measurements; J.F., W.W. and Y.G. performed the confocal PL mapping and power-dependent PL characterizations to confirm the edge

states; Yishi W. carried out transient absorption measurements under the guidance of H.F.; B.Z. performed wettability simulation. J.F., C.G., Yuchen W., L.J. and X.Z. analysed data; J.F., C.G. and Yuchen W. wrote the manuscript. C.G. and X.Z. provided insights into the physical mechanisms. Yuchen W. and X.Z. guided the work. All authors discussed the results and commented on the manuscript.

Competing interests

The authors declare no competing interests.

Additional information

Supplementary information is available for this paper at https://doi.org/10.1038/s41928-018-0101-5.

Correspondence and requests for materials should be addressed to Yuchen W. or H.F. or X.Z.